Tryptophan regulates *Drosophila* zinc stores

Erika Garay[a,1] , Nils Schuth[b,1] , Alessandra Barbanente[c] , Carlos Tejeda-Guzmán[a] , Daniele Vitone[c] , Beatriz Osorio[a] , Adam H. Clark[d] , Maarten Nachtegaal[d] , Michael Haumann[e] , Holger Dau[e] , Alberto Vela, Fabio Arnesano[c,2] , Liliana Quintanar[b,2] , and Fanis Missirlis[a,2]

Zinc deficiency is commonly attributed to inadequate absorption of the metal. Instead, we show that body zinc stores in *Drosophila melanogaster* depend on tryptophan consumption. Hence, a dietary amino acid regulates zinc status of the whole insect—a finding consistent with the widespread requirement of zinc as a protein cofactor. Specifically, the tryptophan metabolite kynurenine is released from insect fat bodies and induces the formation of zinc storage granules in Malpighian tubules, where 3-hydroxykynurenine and xanthurenic acid act as endogenous zinc chelators. Kynurenine functions as a peripheral zinc-regulating hormone and is converted into a 3-hydroxykynurenine–zinc–chloride complex, precipitating within the storage granules. Thus, zinc and the kynurenine pathway—well-known modulators of immunity, blood pressure, aging, and neurodegeneration—are physiologically connected.

zinc homeostasis | pigment granules | synchrotron | lysosome-related organelles | COVID-19

Significance

Zinc deficiency in the human population, a major public health concern, can also be a consequence of nutritional deficiency in protein uptake. The discovery that tryptophan metabolites 3-hydroxykynurenine and xanthurenic acid are major zinc-binding ligands in insect cells establishes the kynurenine pathway as a regulator of systemic zinc homeostasis. Many biological processes influenced by zinc and the kynurenine pathway, including the regulation of innate and acquired immune responses to viral infections, have not been studied in light of the direct molecular links revealed in this study.

Animals distribute metal ions through their circulatory systems to peripheral organs. Systemic regulation of metal homeostasis has been described in the case of iron (Fe), where metal sensing takes place in the liver, an organ that releases the peptide hormone hepcidin when transferrin saturation is high (1). Hepcidin, in turn, binds to the plasma membrane Fe exporter ferroportin, thus down-regulating cellular Fe export and resulting in reduced Fe entry into the circulation and induction of ferritin intracellularly for Fe storage (2). Although a similar process is expected to regulate systemic zinc (Zn) homeostasis, little is known beyond the participation of two intensively studied families of Zn transporters (3). These transporters are evolutionarily conserved and function in Zn trafficking in the dipteran fly *Drosophila melanogaster* (4, 5). In this model organism, a pH-sensitive, Zn-gated chloride channel mediates the coupling of dietary Zn availability to feeding behavior in an insulin-dependent manner (6). Flies avoid high concentrations of Zn, except under conditions of Zn deficiency, which is communicated through the direct action of the glucagon-like adipokinetic hormone on the taste neurons mediating metal sensing (7). Thus, the insulin–glucagon axis is modulated in *D. melanogaster* by systemic Zn availability, as previously suggested for mammals (8). Furthermore, a role for microbiota-dependent Zn provision has been shown, whereby a metabolically active strain of *Acetobacter pomorum* could rescue *D. melanogaster* larvae growing on Zn-deficient media (9). Importantly, heat-inactivated *A. pomorum* could rescue larval growth on Fe- and copper-deficient media but not so for Zn, suggesting that the production of a microbial metabolite could be key for intestinal Zn absorption (9).

Insects concentrate Zn in specialized lysosome-related organelles (LROs) of Malpighian tubule (MT) principal cells (10–12). The biogenesis of LROs has been studied extensively in pigment cells of the eye, starting with the discovery of the *white* (*w*) mutant fly by Thomas Hunt Morgan in 1910 and followed by a substantive number of investigations that have collectively defined the field of animal genetics (13–18). The initial biosynthetic steps of brown ommochrome eye pigments, formed through the degradation of tryptophan (Trp) via kynurenine (kyn) intermediates, occur in larval fat bodies (FBs) and MTs (Fig. 1*A*). Given that *w* and *scarlet* mutants fail to store 3-hydroxykynurenine (3HK) (17)—because they encode for ABCG2-like transporters that dimerize to transport 3HK into autofluorescent granules (16, 19, 20)—and lack Zn storage granules (12), we asked whether mutations in the structural genes of the ommochrome pathway, encoding for enzymes of Trp catabolism, affected Zn accumulation in *D. melanogaster* adult flies. We studied mutants in the Trp dioxygenase *vermilion* (*v*), kyn monooxygenase *cinnabar* (*cn*), kyn aminotransferase (*kyat*), and phenoxazine synthase *cardinal* (*cd*) genes.

Results

The v^1, v^{36f}, cn^{35k}, cn^1, and $kyat^{e299}$ mutants showed 61, 53, 49, 29, and 27% decreases, respectively, in total body Zn normalized to phosphorus (P) compared with the w^+ control flies (Fig. 1*B*). In contrast, Fe (Fig. 1*C*) and other metals (Dataset S1)
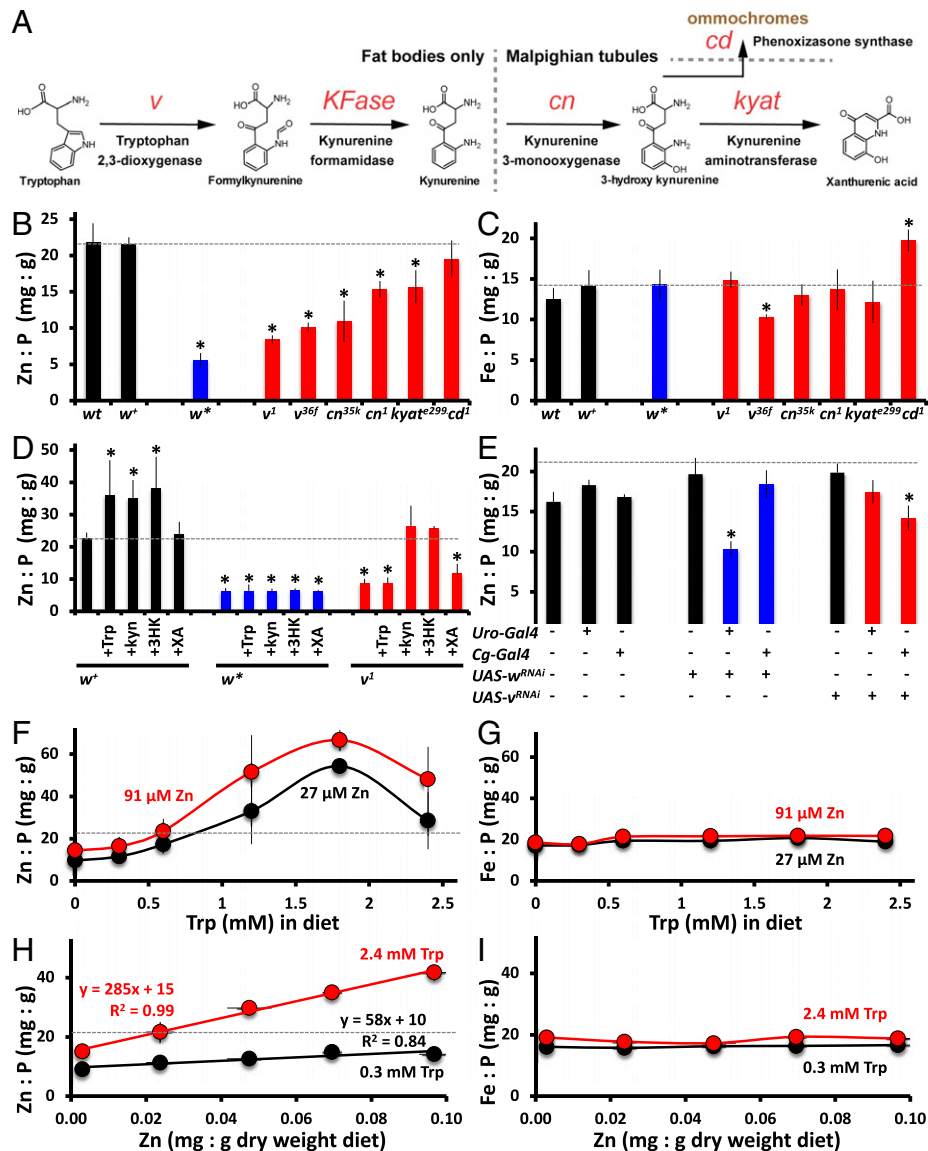
Fig. 1. Trp catabolism regulates Zn storage in the MTs of *D. melanogaster*. (*A*) *Drosophila* genes implicated in the kyn pathway are shown in red, and encoded enzymes are in black. Dotted lines delineate the organs where these genes are primarily expressed. (*B*) Zn content normalized to P in adult flies of mixed sex. Control wild-type (*wt*) and w^+ genotypes are indicated in black. The gray dotted line indicates the normal concentration of Zn at ~21 mg Zn/g P. Blue indicates the isogenic *w** stock ; red indicates the v^1, v^{36f}, cn^1, cn^{35k}, $kyat^{e299}$, and cd^1 mutants ([Dataset S1](#)). (*C*) Fe content in the same genotypes indicates the specificity of the changes in Zn since Fe showed no consistent changes in the same samples. (*D*) The effect on the Zn/P ratio following dietary supplementation of 2.4 mM Trp, kyn, 3HK, or XA to the w^+, *w**, and v^1 mutants. (*E*) The effect of tissue-specific RNAi on the Zn/P ratio. Blue bars indicate knockdown of the *w* gene, and red bars indicate knockdown of the *v* gene. The *Uro-Gal4* transgene was used to drive RNAi specifically in the MTs, whereas *Cg-Gal4* was for the FBs (crosses indicate the presence of transgene) (full genotypes and replicate measurements are given in [Dataset S1](#)). Statistical treatment of results was with one-way ANOVA ($\alpha = 0.01$) followed by Tukey's test for differences between groups. For simplicity, asterisks in *B–D* indicate statistical difference to the w^+ control group in black bars, and in *E*, they indicate statistical difference to the respective uninduced RNAi strain. (*F*) Dietary Trp concentration during larval growth regulates Zn content in adult flies. Larvae were grown on chemical media with defined concentrations of Zn (red and black lines, respectively) and Trp (*x* axis). Elemental analysis of whole flies using inductively coupled plasma optical emission spectrometry was performed, and the Zn/P ratio is shown on the *y* axis. (*G*) Fe/P ratio in the same samples as in *F*. (*H*) In this experiment, larvae were grown on chemically defined media with high or low Trp (red and black lines, respectively), while the Zn concentration was varied and determined experimentally on the *x* axis. The equations describe a linear fit to the data. (*I*) Fe/P ratio in the same samples as in *H*.

showed no consistent change between the same samples. The cd^1 mutant showed no significant difference of relative Zn concentration to controls (Fig. 1*B*), a finding compatible with expression of the *cd* gene in the developing eye (Fig. 1*A*). These results implicated the kyn pathway in the regulation of Zn storage and/or excretion in *Drosophila*.

We performed dietary rescue experiments (20) to demonstrate the relevance of Trp metabolites in organismal Zn storage (Fig. 1*D*). Dietary supplementation of 2.4 mM Trp had no effect when administered to the v^1 mutant, as expected for flies that do not metabolize this amino acid down the kyn pathway.

In contrast, 2.4 mM kyn or 3HK fully corrected the low Zn phenotype of the v^1 mutant (from 38 to ~115% of wild-type Zn content), whereas 2.4 mM xanthurenic acid (XA) had a small effect (38 to 52%). Neither compound had any effect on the *w** mutant (Fig. 1*D*). Surprisingly, supplementation of Trp, kyn, and 3HK to control w^+ flies resulted in 57, 54, and 67% increases, respectively, in their body Zn content (Fig. 1*D*). These results suggested that Trp and its downstream metabolites directly regulate Zn storage in the MTs in a manner that is dependent on the action of the *w* gene since the same compounds have no impact on the diminished Zn
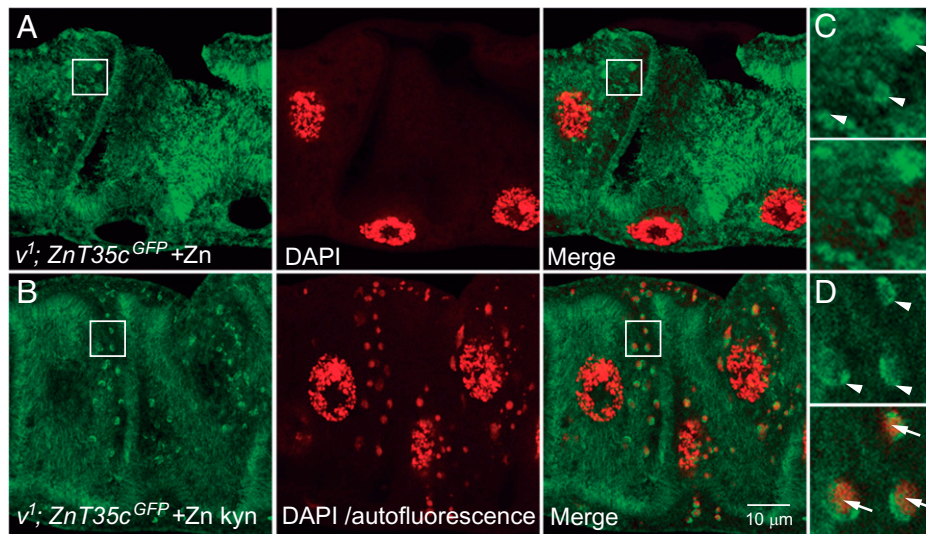
Fig. 2. Kyn induces the formation of Zn storage granules in principal cells of *D. melanogaster* MTs. (*A*) Confocal image of the transitional segment of the anterior MT from v^1 mutant larvae expressing the ZnT35C–GFP transgene (green) after 24 h of incubation in diet supplemented with 1 mM Zn sulfate. Nuclei of dissected tubules were stained with DAPI (false-colored red); the combined signal is also shown (merged image). (*B*) Confocal images taken from the v^1 mutant larvae expressing the ZnT35C–GFP after 24 h of incubation on media with 1 mM Zn sulfate and 2.4 mM kyn; the combined treatment leads to the appearance of autofluorescent material (visible upon ultraviolet excitation) inside ZnT35C–GFP-positive organelles. (*C* and *D*) Higher magnification of the boxed areas in *A* and *B*. Arrowheads point to organelle-like structures positive for ZnT35C–GFP. Arrows point to autofluorescent organelles. Note that in *D*, ZnT35C–GFP is present on one side of the organelle-like structures.

concentration of *w* mutant animals that fail to transport 3HK (16) into granules (19) and fail to form Zn storage granules (12). Next, to demonstrate that the *v* gene was acting in the FBs, as first envisioned already in 1936 (14), we used RNA interference (RNAi) to knock down *v* and *w* in FBs and MTs, respectively. RNAi against the *w* gene in the MTs resulted in reduced Zn concentration in the flies, whereas the same manipulation in the FBs had no effect (Fig. 1*E*). The opposite was observed with *v* RNAi, which lowered Zn concentration only when directed to the FBs but had nonsignificant effect in the MTs. Our results corroborate the findings from previous work showing that kyn is synthesized in the FBs and trafficked to the MTs (16, 20) and extend these observations to include Zn accumulation in the MTs as a response to kyn, derived from the FBs.

To examine in more detail the relationship between dietary Zn and Trp on organismal Zn retention in the MTs of *D. melanogaster*, we used chemically defined media and varied the concentration of Trp in diets containing 27 and 91 µM Zn acetate (Fig. 1*F*); for comparison, standard yeast–molasses-based diet contains ∼50 µM Zn (21). This experiment revealed that the major determinant for Zn storage in flies was Trp concentration in the media, with a peak for Zn accumulation at a concentration of 1.8 mM Trp. Thus, a threefold difference in dietary Zn within a physiologically relevant range had only a small effect on body Zn stores, which were instead primarily determined by Trp concentration, also varied within a custom range in our experiments (22). The specificity of the Trp effect on Zn was demonstrated with the parallel measurements of Fe in these samples (Fig. 1*G*) showing no changes in this metal ion and by testing supplementation of other amino acids, such as glutamate, glycine, phenylalanine, and histidine, none of which affected total body Zn concentration (*SI Appendix*, Fig. S1 *A* and *B*). The presence of kyn in the diet did not alter the feeding behavior of w^+ and v^1 larvae, although mutant v^1 larvae consumed less food (*SI Appendix*, Fig. S1 *C–E*). The interaction between Trp and Zn was further corroborated in experiments where dietary Zn was varied under high (2.4 mM) or low (0.3 mM) Trp concentration (Fig. 1*H*). In the presence of

2.4 mM Trp, a linear relationship between dietary and organismal Zn is observed, whereas when Trp is limited to 0.3 mM, dietary Zn does not accumulate efficiently in flies. Once again, Fe did not change as a function of dietary Zn (Fig. 1*I*). Considering earlier reports of an effect of Trp on Zn absorption in animals and humans (23), it is possible that Zn deficiency in humans and animals (24, 25) could also be the result of reduced protein (Trp) intake.

To describe at the cellular level the relationship between kyn and Zn storage granules, we used a green fluorescent protein (GFP) fused to the Zn transporter ZnT35C as a marker (12). For these experiments, we worked with the larval stages of development based on prior descriptions of autofluorescent granules in their MTs (20). We confirmed that Zn concentrates in the MTs of w^+ larvae, as previously shown for adults (12), and that the v^1 and w^* mutants had trace amounts of Zn in this organ (*SI Appendix*, Fig. S2*A*). In MTs from control w^+ larvae placed for 24 h on medium supplemented with 1 mM Zn sulfate, we observed ZnT35C–GFP expression in principal cells on the tubule main segment (*SI Appendix*, Fig. S2*B*). The transporter was not detected in the distal region of the tubules where manganese and calcium accumulate (26, 27), although the few cells that connect these two regions (transitional segment) had the highest expression (*SI Appendix*, Fig. S2*B*). The v^1 mutant larvae showed significant expression of ZnT35C–GFP localized in cellular membranes but no presence of autofluorescent granules (Fig. 2*A*). When the v^1 mutant larvae were placed for 24 h on media supplemented with 1 mM Zn sulfate and 2.4 mM kyn, Zn storage granules of ∼1.5 µm in diameter were now formed (Fig. 2*B*). Autofluorescent granules contain Zn based on the Fluozin3 reporter (*SI Appendix*, Fig. S2*C*). The fluorescent spectrum registered directly from the granules (excitation at 405 nm) peaked around 510 nm (*SI Appendix*, Fig. S3). These experiments were also performed ex vivo to enable the direct application of kyn to culture MTs, further corroborating that kyn produced in the FBs induces the formation of Zn storage granules in MT principal cells while also down-regulating ZnT35C expression (*SI Appendix*, Fig. S2*D*).

The observed increase in fly Zn content upon exposure to dietary Trp or its kyn derivatives could be potentially explained if a Trp metabolite directly chelated Zn and the complex accumulated in the granules. To evaluate Zn coordination in situ, we used Zn K-edge X-ray absorption spectroscopy (XAS), as previously performed in isolated cells (28, 29). Control w^+ and v^1 mutant second instar larvae were placed on diets with or without 2.4 mM kyn, and the MTs were dissected 72 h later from wandering third instar larvae. X-ray absorption near-edge structure (XANES) and extended X-ray absorption fine structure (EXAFS) spectra were collected at the KMC-3 beamline at the light source BESSY II (former Berliner Elektronenspeicherring-Gesellschaft für Synchrotronstrahlung m.b.H., now Helmholtz-Zentrum Berlin für Materialien und Energie) in Germany and the SuperXAS beamline at the Swiss Lightsource (SLS) in Switzerland, obtaining comparable results (*SI Appendix*, Fig. S4), while no radiation damage was observed (*SI Appendix*, Fig. S5). The lack of Zn storage granules in v^1 MTs resulted in a >90% decrease in unnormalized XANES intensity (*SI Appendix*, Fig. S6) and a significant change in normalized XANES and EXAFS compared with w^+ MTs (Fig. 3 *A* and *B*). However, XAS of whole Malpighian tubule protein purification (MTP) from w^+ shows only small differences from v^1 MTs. Additionally, MTs of v^1 grown with kyn-supplemented diet yielded virtually indistinguishable XANES spectra from those of MTs from w^+. Thus, 1) Zn present in v^1 MTs is almost entirely protein bound, and 2) additional Zn found in w^+ is very likely present as small inorganic compounds deriving from kyn metabolites.

To verify which metabolites are present in Zn storage granules, we performed Zn K-edge XAS on Zn compounds with kyn metabolites. For this analysis, XAS spectra were collected of the Zn complexes with XA (XA–Zn) and 3HK (3HK–Zn) in the solid state (Fig. 3 *C* and *D*). Using the XANES (Fig. 3*E*) and EXAFS (Fig. 3*F*) regions of XA–Zn, 3HK–Zn, and MTP, we were able to create composite spectra superimposable to w^+ MTs. Similar results were obtained when the MTP spectrum was replaced with that of v^1 MTs (*SI Appendix*, Fig. S7). In essence, adding spectra from 3HK–Zn and XA–Zn to spectra from samples lacking Zn storage granules has the same effect as adding kyn to the diet of v^1 larvae. The spectral composition analysis revealed that the 3HK–Zn and XA–Zn complexes are present in a 5:1 relation (*SI Appendix*, Table S1). These results strongly suggest that Zn is bound to 3HK in the storage granules and to a smaller extent to XA.

To identify the chemical nature of Zn complexes with kyn metabolites, solution studies were performed using electronic absorption, electrospray ionization mass spectrometry (ESI-MS), and nuclear magnetic resonance (NMR) (*SI Appendix, SI Text* and Figs. S8–S19). A solution of 3HK was initially titrated with ZnCl$_2$ up to one equivalent in deuterated dimethyl sulfoxide (DMSO-d$_6$), due to the higher solubility of the free ligand in a polar aprotic solvent, as compared with water. The ESI-MS spectrum of this solution recorded in negative ion mode displayed a main signal at a mass to charge ratio (m/z) 358.9393 that corresponds to the singly charged species $[C_{10}H_{11}ClN_2O_4Zn + Cl]^-$ (*SI Appendix*, Fig. S8A), indicating that the Zn ion coordinates to a 3HK molecule and a chloride ion in a 1:1:1 ratio. The complex obtained at the end of the titration yielded a nearly identical XAS spectrum to that of the solid compound (3HK–Zn) (*SI Appendix*, Fig. S17A). Comparison between one-dimensional (1D) ^{13}C NMR spectra of free 3HK and 3HK–Zn–Cl in dimethyl sulfoxide (DMSO) (*SI Appendix*, Fig. S9A) and in water (Fig. 4A) showed that all ^{13}C signals in the aliphatic portion of

the molecule experienced dramatic broadening in the presence of Zn, while aromatic signals were only marginally affected. Displacement of two-dimensional (2D) ^{1}H-^{13}C heteronuclear single quantum coherence (HSQC) cross-peaks was observed for CH and CH$_2$ groups at positions 2 and 3, while aromatic signals remained unperturbed (*SI Appendix*, Fig. S10A). NMR results and structural analysis indicate that the aliphatic amine is the preferred binding site and allows Zn chelation by the carboxylate and the carbonyl group. Indeed, ab initio density functional theory (DFT) studies of a 3HK–Zn–Cl complex with this coordination sphere yielded a structure with metal–ligand distances that are consistent with those experimentally determined by EXAFS analysis (Figs. 3*D* and 4*C* and *SI Appendix*, Tables S2 and S3). Hence, the best structural model for the 3HK–Zn–Cl complex is a nearly tetrahedral structure where the Zn ion is coordinated by the carboxylate in a monodentate fashion, the aliphatic amine, and carbonyl groups, while a chlorine ion acts as a fourth ligand (*SI Appendix*, Fig. S18*A* and *SI Text*), which is in line with the observed sharp (1s → 4p orbital) XANES transition (29). The facts that L-kynurenine, lacking a phenol group, forms the same type of adduct as 3HK (i.e., L-kyn–Zn–Cl) (ESI-MS in *SI Appendix*, Fig. S8 *C* and *D* and NMR data in *SI Appendix*, Fig. S9*B*) and that the ultraviolet-visible electronic absorption and fluorescence emission spectra of 3HK are insensitive to Zn(II) addition (*SI Appendix*, Fig. S10 *B*–*E*) confirm that the 2-aminophenol moiety is not involved in Zn binding.

On the other hand, titration of a solution of XA in D$_2$O with ZnCl$_2$, monitored by 1D ^{1}H NMR, showed that all spectral changes stopped at 0.5 equivalents of Zn, indicating the formation of a complex with a 2:1 XA/Zn stoichiometry (*SI Appendix*, Fig. S11). Consistently, the ESI-MS spectrum of Zn(XA)$_2$ in basic aqueous solution recorded in positive ion mode showed a main peak at m/z 472.9956 corresponding to the singly charged species $[C_{20}H_{12}N_2O_8Zn + H]^+$ (*SI Appendix*, Fig. S12). The spectrum obtained at the end of the titration was again nearly identical to that of the synthesized Zn(XA)$_2$ compound dissolved in D$_2$O under the same conditions, as assessed by NMR (*SI Appendix*, Fig. S11) and XAS (*SI Appendix*, Fig. S17*B*). Combined, 1D ^{13}C NMR (Fig. 4*B*) and 2D ^{1}H-^{13}C HSQC (*SI Appendix*, Fig. S13*A*) spectra of free XA and Zn(XA)$_2$ show that the carboxylate carbon and the carbon atoms near the quinolinic nitrogen and phenol group are the most perturbed upon Zn binding. The large upfield shift of the distant atom C4 is ascribed to the tautomeric transformation from the keto to the enol form of the ligand at alkaline pH (30), prompted by Zn chelation. DFT studies yielded a structural model for the Zn(XA)$_2$ complex where the metal ion is coordinated by the quinoline nitrogen and the carboxylate group of each ligating XA, while a hydrogen bond between the carboxylate of one XA molecule and a phenyl hydroxyl group of a second XA stabilizes the complex at neutral pH (Fig. 4*D* and *SI Appendix*, Fig. S18*B*). This structural model for the Zn(XA)$_2$ complex displays metal–ligand distances that are consistent with those experimentally determined by EXAFS analysis (Figs. 3*D* and 4*D* and *SI Appendix*, Tables S2 and S3) and a distorted square planar geometry in agreement with the lower XANES peak height (29). Additionally, XA displays two pK$_a$ values (pK$_a$ = -log$_{10}$ K$_a$ acid dissociation constant), pK$_{a,1}$ = 2.5 and pK$_{a,2}$ = 7.55 (*SI Appendix*, Fig. S14), corresponding to the carboxylic and phenol/quinoline nitrogen groups, respectively (*SI Appendix, SI Text*). Upon Zn binding, the pK$_{a,2}$ downshifts to 7.2, suggesting a small percentage (10%) of a second deprotonated species where the phenyl hydroxyl group coordinates the metal ion at physiological pH (*SI Appendix*, Fig. S14).
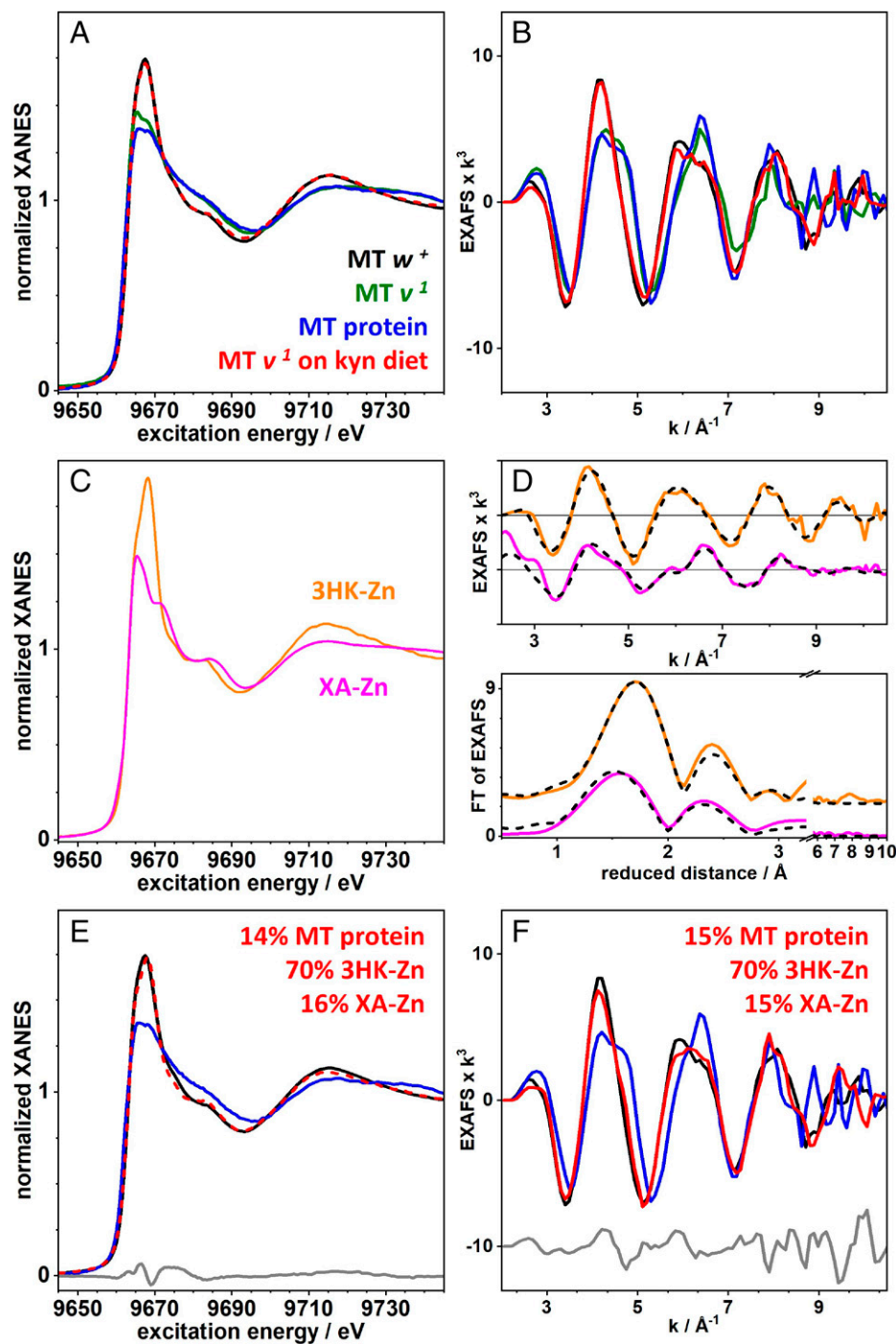
Fig. 3. The chemical environment of Zn in whole wild-type MTs as revealed by Zn K-edge XAS is consistent with the accumulation of 3HK–Zn and XA–Zn complexes when Zn storage granules are formed. (*A*) Normalized Zn K-edge XANES and (*B*) EXAFS are shown from w^+ MTs (black), v^1 MTs (green), and purified protein from w^+ MTs (blue). The red spectra stem from v^1 MTs from animals fed for 72 h on diet supplemented with 2.4 mM kyn. (*C*) Zn K-edge XANES, (*D, Upper*) EXAFS, and (*D, Lower*) FT are shown from 3HK–Zn–Cl (orange) and Zn(XA)$_2$ (pink). Black dashed lines correspond to fits of corresponding EXAFS spectra using simulation parameters given in *SI Appendix*, Table S2. (*E*) Spectral composition of XANES and (*F*) EXAFS from purified protein from w^+ MTs, 3HK–Zn–Cl, and Zn(XA)$_2$ (red) is superimposable to the w^+ MT spectrum (black), suggesting that the Zn storage granules accumulate the two complexes that are lacking in the purified proteins from w^+ MTs or in the v^1 mutant (*SI Appendix*, Fig. S7). The spectrum from purified protein from w^+ MTs (blue) is shown for comparison. The respective weight of spectral composition is indicated, and differences between the composition and w^+ MTs are also shown (gray).

Indeed, considering this second species improves the EXAFS fit (Fig. 3*D*), while changes in bond distances upon deprotonation are in good agreement between DFT and EXAFS.

Zn binding to XA causes a significant fluorescence enhancement at 590 nm upon excitation at 368 nm for pH values between 12 and 7 (*SI Appendix*, Fig. S13 *B–G*). At acidic pH, no increase in fluorescence was detected, consistent with the lack of Zn binding as confirmed by NMR analysis (*SI Appendix*, Fig. S16 and *SI*

Text). The apparent dissociation constants ($K_{d,app}$) of the Zn(II) complexes with 3HK and XA were estimated by competition assays with Zincon [2-carboxy-2'-hydroxy-5'-(sulfoformazyl)benzene], a colorimetric Zn sensor that forms a 1:1 complex with Zn^{2+} having a distinct absorption band at 620 nm and a $K_{d,app}$ of $5.8 \cdot 10^{-6}$ M (31). Experiments with Trp metabolites were performed at two different pH values, 7.5 (10 mM 2-[4-(2-Hydroxyethyl)piperazin-1-yl]ethane-1-sulfonic acid (Hepes), 100 mM NaCl)

and 9.0 (50 mM sodium borate). Titration of Zn–Zincon with 3HK showed a tight isosbestic point at 530 nm at both pH values, consistent with a clean 1:1 reaction (*SI Appendix*, Fig. S19 *B and E*). In the case of XA, loose isosbestic points were observed at both pH values, indicative of a two-stage reaction with little accumulation of the 1:1 complex (32) (*SI Appendix*, Fig. S19 *C and F*). Half-maximal absorption at 620 nm was achieved after the addition of about 15 equivalents of 3HK and 2 equivalents of XA at pH 9. Data analysis allowed us to estimate dissociation constants in the high micromolar range for Zn–3HK–Cl ($K_{d,app} \sim 6.4 \cdot 10^{-5}$ M) and in the low micromolar range for the 1:2 complex $Zn(XA)_2$ ($K_{d,app} \sim 1.8 \cdot 10^{-10}$ M^2) at pH 7.5 (*SI Appendix, SI Text*).

Discussion

In summary, XAS studies demonstrate that the portion of total Zn present in MT primary cells that is associated with the formation of the Zn storage granules is bound to 3HK and XA. The chemical nature of these Zn complexes could be elucidated using a combination of spectroscopic tools and DFT calculations. The $Zn(XA)_2$ complex shown in Fig. 4*D* and its deprotonated form (*SI Appendix*, Fig. S18*C*), which is a minor species, together constitute one-sixth of the Zn complexes, while the predominant species (>80%) is the 3HK–Zn–Cl complex shown in Fig. 4*C*.

Drawing parallels to systemic Fe metabolism (2), the Zn storage granule has a ferritin-like function. In conditions where bloodstream Fe is abundant, the liver releases hepcidin to down-regulate ferroportin, thus excluding Fe from the circulation, while ferritin stores Fe intracellularly until homeostasis is reached (2). We showed that kyn from *D. melanogaster* FBs is required for Zn storage granule formation in MTs and furthermore, that kyn down-regulates ZnT35C (*SI Appendix*, Fig. S2*D*), the transporter that has been implicated in Zn storage (12) and excretion (5, 33). Both actions of kyn resemble those of hepcidin in systemic Fe regulation (2). Kyn has been long considered a hormone in insects (14, 34, 35) and ecdysozoa more generally (36). Last but not least, liver hepcidin is independently induced during inflammation. Kyn and XA have known immunoregulatory properties (37–39) that could be related to a similar immunomodulation attributed to systemic Zn availability (40).

Zn absorption in humans and other mammals has been related to a small molecule secreted by both the pancreas and the mammary gland, whose identity was sought and debated extensively 40 y ago (23). The demonstration that Trp affected Zn absorption (or its retention) in the rat intestine led to the consideration of a high-affinity Zn ligand, picolinic acid (23, 41). Involvement of this metabolite in Zn homeostasis was challenged at the time on the basis that Trp had more potent
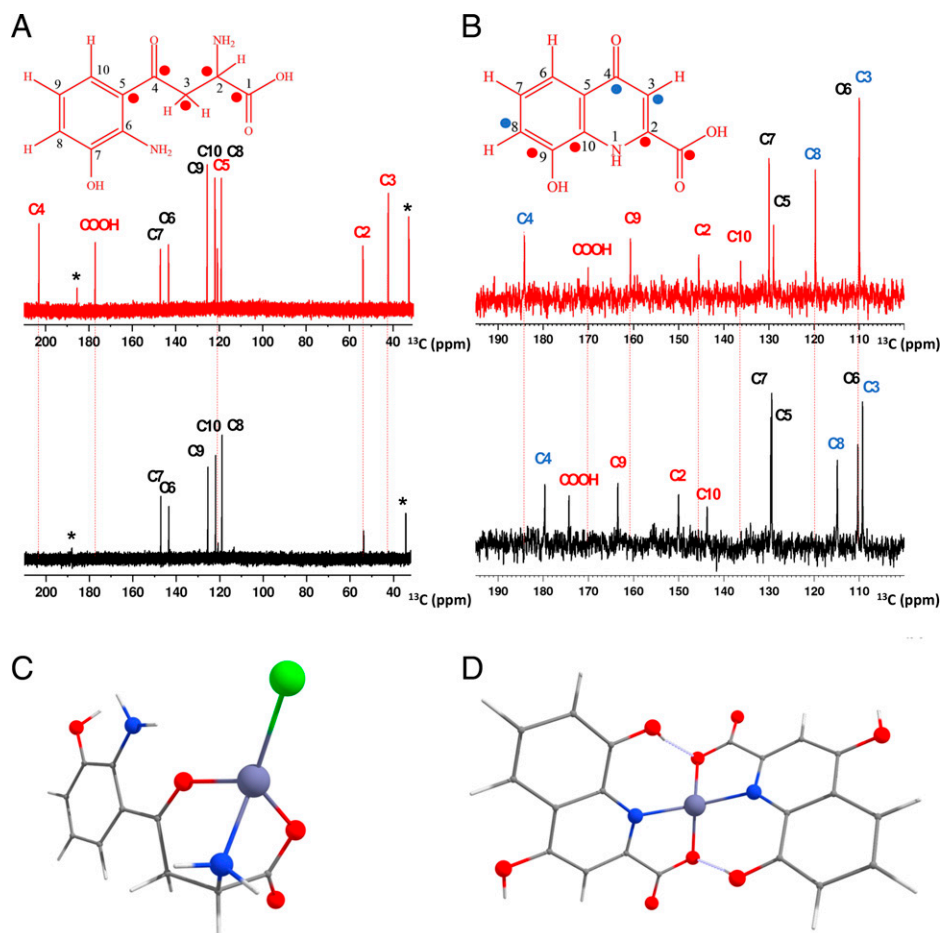

Fig. 4. (*A*) The 1D ^{13}C spectra of free 3HK (red contours) and 3HK–Zn–Cl (black contours) in H_2O/D_2O 90:10% (pH 4.7). (*B*) The 1D ^{13}C spectra of free XA (red contours) and $Zn(XA)_2$ (black contours) in D_2O (pD 12.3). The structural formulas with atom numbering are shown in *A, Upper* and *B, Upper*. ^{13}C signals downfield shifted or exchange broadened upon Zn binding are marked with red dots, and ^{13}C signals upfield shifted upon Zn binding are marked with blue dots. The assignment is indicated on the top of each peak. The ^{13}C signals of TSP are marked with asterisks. DFT-derived structures for the Zn complexes with kyn metabolites (*C*) 3HK–Zn and (*D*) $Zn(XA)_2$. Structures were derived with the Becke and Perdew generalized gradient exchange-correlation (BP) functional and in implicit solvation. *SI Appendix*, Fig. S18 and Table S3 show metal–ligand distances, Dataset S2 has Cartesian coordinates, and *SI Appendix, SI Text* has detailed considerations.

effects than those observed with picolinic acid and moreover, that picolinic acid was a trace catabolite of the Trp degradation pathway (42). A dissociation constant of Zn in the high micromolar range for 3HK (*SI Appendix*, Fig. S19) is consistent with the concentration of this metabolite (43) and of Zn (10) in the Zn storage granule. Hence, outside of the specialized context of acidified granules, chelation of the metal ion by 3HK is unlikely. Conversely, XA has a higher affinity for Zn in neutral pH but does not bind the metal in acidic medium (*SI Appendix*, Figs. S13 and S16). These findings suggest that the two Trp metabolites are likely involved in Zn binding in microenvironments of variable pH and metal ion content, which may arise during the maturation and turnover of the Zn storage granule (44, 45).

The possibility that the kyn pathway modulates Zn uptake through the intestine should not be excluded. In this light, the suggestion that Zn absorption in *D. melanogaster* is facilitated by live intestinal microbiota is highly intriguing (9). A similar finding was also shown for symbiotic bacteria of the louse fly *Melophagus ovinus* (46). Indeed, it is well established that microbiota regulate the kyn pathway (47) and vice versa, that genetic interference with indoleamine 2,3-dioxygenase (homologous to *v*) alters the microbiota (48). It remains to be investigated if metabolic modulation of Trp metabolites relates to Zn mobilization/storage in the host. Sensing of Zn itself in the intestinal lumen of *D. melanogaster* through the gating of a chloride channel and downstream insulin-related signaling could play additional roles in this context (6) and may be related to the observed differences in feeding between w^+ and v^1 larvae (*SI Appendix*, Fig. S1 *D* and *E*), which require further investigation.

The link in *D. melanogaster* metabolism between kyn and Zn suggests that the kyn pathway could also act in concert with Zn beyond the immune system in the vasodilatory system (49–51) of higher animals. Similar connections should be considered for the roles of Zn and kyn in the brain (52, 53), glucose metabolism (54), and during animal aging (55–57). The physiological connection of Trp and Zn makes sense in the light of evolution, considering that Trp is chemically adapted to interact with an oxygen-rich environment (58). The rise of atmospheric oxygen at the skirts of the Phanerozoic eon caused a parallel rise of Zn concentration in the sea and led to the appearance of widely used Zn-containing protein domains, including the Zn fingers (59, 60). Given the significant increase in environmental Zn bioavailability, newly evolving animals co-opted Trp catabolism to store or excrete away excess Zn while also exploiting the metal for enzymatic and structural protein functions. The proposal presented here that the kyn pathway is a systemic regulator of Zn in *D. melanogaster* offers potential insight into the unsolved question of how systemic Zn homeostasis operates in humans with significant repercussions when considering worldwide human Zn deficiency. More urgently, the connection should be considered in the context of the present COVID-19 pandemic (61–67).

Materials and Methods

Chemicals. Tryptophan (T0254), DL-kynurenine (61250), L-kynurenine (K8625), 3-hydroxy-DL-kynurenine (H1771), XA (D120804), Zn acetate (379786), Zn chloride (229997), Zn sulfate (96495), Zn iodide (466360), cadmium chloride (239208), sucrose (S0389), methanol (179337), chloroform (C2432), penicillin (P3032), streptomycin (S9137), Schneider's Insect Medium (S0146), fetal calf serum (F2442), Hepes (H3375), ammonium acetate (A7262), ammonium bicarbonate (09830), boric acid (B0394), dimethyl sulfoxide-d$_6$ (151874), deuterium oxide (151882), and Zincon monosodium salt (96440) were purchased

from Sigma-Aldrich. Metal-free, concentrated (65%) Suprapur nitric acid (1004411000) was from Merck. All chemicals used for the preparation of the defined media are listed in ref. 21 along with a regular diet based on yeast and molasses.

***Drosophila* Stocks.** Wild-type *Tan3* flies, the generation of isogenic w^+ and w^* strains, and the $ZnT35C^{GFP}$ stock are described in ref. 12. Mutant strains v^1 (86542), v^{36f} (142), cn^{35k} (268), cn^1 (263), $kyat^{e299}$ (17840), cd^1 (3052), and *Cg-Gal4* (7011) were obtained from the Bloomington *Drosophila* Stock Center (BDSC). The full genotype for stock 17840 is w^{1118}; $PBac\{RB\}$ $Kyat^{e00299}$; the *PBac* insertion was backcrossed into the w^+ isogenic background. $ZnT35C^{GFP}$ (BDSC; 59419) was placed in w^+ and v^1 backgrounds. The *Cg-Gal4* transgene drives expression in the FBs, and its full genotype is given as w^{1118}; $P\{w^{+mC},$ *Cg-GAL4.A*}2. The *Uro-Gal4* transgene drives expression in the main segment of MT (68) and was donated by Julian A. T. Dow (University of Glasgow, Glasgow, Scotland, United Kingdom). BDSC strains UAS-w^{RNAi} (31088; full genotype: y^1, v^1; $P\{y^{+t7.7}, v^{+t1.8}, TRiP.JF01540\}attP2$) and UAS-v^{RNAi} (50641; full genotype: y^1, v^1; $P\{y^{+t7.7}, v^{+t1.8,} TRiP.HMC03041\}attP2$) were used to drive RNAi for the *w* and *v* genes, respectively. Note that when Gal4 drivers carrying a *w* allele in the X chromosome are crossed to the transgenic RNA interference project (TRiP; Harvard Medical School, Boston, MA) RNAi lines that carry the *y* and *v* alleles (69), all female progeny are heterozygous for the *w*, *v*, and *y* loci. Given that these gene mutations are recessive in character, the heterozygous animals have normal Zn stores in the absence of RNAi effects. Only female flies were used in this experiment (Fig. 1*E*).

Elemental Analysis. Different types of samples were prepared for elemental analysis using inductively coupled plasma optical emission spectrometry. For RNAi experiments, female flies of the indicated genotype were collected between an age of 4 and 7 d old. For other whole-fly experiments, mixed sex populations were used of the same age period. The different diets were first cut into small cubes. Animals or diet cubes were freeze dried for 8 h to remove water. Twenty milligrams of dry sample was digested in 1 mL of concentrated (65%) metal-free Suprapur nitric acid at 200 °C for 15 min in closed vessels of the MARS6 microwave digestion system (CEM Corporation). Samples were diluted with Milli-Q water to 5 mL. Metal concentrations were measured against calibration curves and a digestion blank in a PerkinElmer Optima 8300 instrument. Calibration curves were performed for copper, manganese between [0.02 to 1 ppm]; Fe, Zn [0.1 to 5 ppm]; calcium, magnesium [0.5 to 25 ppm]; sodium [1 to 50 ppm]; and potassium, P [2 to 100 ppm]. All elemental measurements were within the verified linear range of the respective calibration curves.

Sample Preparations for Confocal Microscopy. Flies of the genotypes w^+; $ZnT35C^{GFP}/CyO$ and v^1; $ZnT35C^{GFP}/CyO$ were allowed to lay their eggs on regular yeast–molasses diet at 25 °C. Approximately 15 second instar stage larvae were transferred to vials containing 5 mL of conventional yeast–molasses-based food (21) supplemented with 1 mM Zn sulfate and 2.4 mM kynurenine as indicated. After 24 h, larvae were dissected; MTs were collected in phosphate-buffered saline (PBS), treated with 4% paraformaldehyde for 10 min, and washed in PBS, and all nuclei were stained with 4′,6-diamidino-2-phenylindole (DAPI) before mounting to slides for observations. Confocal images were obtained by using a Zeiss LSM510 system and processed using ImageJ. Autofluorescence emission was determined between 413 and 471 nm with excitation at 405 nm.

MT Preparations for Synchrotron Analysis. MTs from 22 third instar larvae fed during 72 h with conventional yeast–molasses-based food (21) supplemented with 2.4 mM Trp or kyn were dissected in a 0.25 M sucrose solution. Each pair of tubules was transferred rapidly to a drop of 0.25 M sucrose placed in a Kapton-covered acrylic glass holder. The sealed holders were frozen in liquid nitrogen and transported to the synchrotron in a prechilled dewar.

Whole MTP for Synchrotron Analysis. Seventy pairs of MTs were homogenized at 4 °C in a 0.25 M sucrose solution using a plastic pestle for 60 s. The homogenate was centrifuged at 1,000 × g for 10 min at 4 °C to remove cell debris and nuclei. The supernatant was recentrifuged at 8,000 × g for 15 min to get a soluble fraction, which was used for methanol and chloroform protein precipitation. Finally, the precipitated proteins were lyophilized in a Labconco freeze-dry system and shipped as frozen powder to the synchrotron X-ray source.

The frozen powder was placed in a Kapton-covered acrylic glass holder, sealed, and frozen in liquid nitrogen.

Chemical Synthesis. XA–Zn was prepared as previously reported (70). Briefly, 0.205 g of XA was dissolved in 20 mL of water. Upon addition of 10 mL of 0.1 N NaOH, the solution was filtered with filter paper; 0.068 g of $ZnCl_2$ was added, and the pH was adjusted to pH 5.8 or 9.4. The solution was heated for 10 min at 80 °C, and XA–Zn was purified and dried. The 3HK–Zn complex was prepared by mixing predissolved 3HK with $ZnCl_2$ in 30 mL of water in a 2:1 molar ratio. The newly formed 3HK–Zn complex was observed after the addition of 12 mL of 0.1 N NaOH. The pH was adjusted to 4.5, and the 3HK–Zn complex was collected, washed, and dried. Ten milligrams of each powder was mixed with 90 mg of boronitrate and pressed into a pellet prior to measurement at the SuperXAS beamline at the SLS. The purity of $Zn(XA)_2$ was verified by elemental analysis, whereas 3HK–Zn–Cl was a minor component in solid state mixed with precipitated free ligand (*SI Appendix, SI Text*).

XAS Data Collection and Analysis. XAS at the Zn K-edge was performed at beamline KMC-3 at BESSY-II (Berlin, Germany) using the previously described setup: storage ring operated in top-up mode at 300 mA, double-crystal Si[111] monochromator with an ~2-eV bandwidth, 13-element energy-resolving silicon-drift detector (RaySpec) for fluorescence monitoring, and sample held in a cryostat (Oxford) at 20 Kelvin (71). The X-ray spot size on the sample was set by a focusing mirror and slits to about 4.0×1.5 mm. Signal-to-noise ratios were improved by averaging of spectra collected on the only sample spots. Photodamage was not observed, as expected for the Zn(II) species (*SI Appendix,* Fig. S3). XAS spectra were averaged after detector dead time and self-absorption correction and normalized to derive XANES spectra, and EXAFS spectra were extracted as described earlier (72). XAS at the Zn K-edge was also performed at the synchrotron SLS (Villigen, Switzerland) at the SuperXAS superbending-magnet beamline with the storage ring operated in top-up mode (400 mA) using a setup for XAS as previously described (73). A channel-cut Si[111] monochromator was used for scanning of the excitation energy. The X-ray spot size on the sample was set by slits to about 1.5×0.3 mm. Fluorescence-detected dead time–corrected XAS spectra were measured using an energy-resolving five-elements silicon drift detector (RaySpec), which was shielded by 10-µm Cu foil against scattered incident X-rays (one scan of ~20-min duration per sample spot). Samples were cooled by a stream of liquid nitrogen vapor at ~100 K. At both beamlines, the monochromator energy axis was calibrated (accuracy ±0.1 eV) using the first inflection point at 9659 eV in the simultaneously measured absorption spectrum of a Zn foil as a standard. Averaging (three to six scans per sample), normalization, and extraction of EXAFS oscillations and conversion of the energy scale to the wave-vector (k) scale were performed as previously described (71). The k^3-weighted EXAFS spectra were simulated ($S_0^2 = 1.00$) by a least-squares procedure using phase functions calculated with FEFF8-lite (74), and Fourier transforms (FTs) were calculated using the in-house software SimX using k range of 2.3 to 11.3 Å^{-1}, with cosine windows extending over 10% at both k-range ends (75, 76). SimX uses the Levenberg–Marquardt (damped least-squares) algorithm. The E_0 used for extraction of EXAFS oscillations was 9660 eV, and E_0 was refined to about 9660 ± 2 eV in the EXAFS fitting (the "error" margin refers to the full E_0 variation range for all analyzed spectra).

NMR Spectroscopy. NMR samples were prepared by dissolving the synthesized complexes and free ligands in H_2O with 10% D_2O (for locking purposes) and in D_2O or DMSO-d_6 at 1 and 4.5 mM concentrations, and the pD (pD = $-log_{10}$ [D^+]) was adjusted with $DClO_4$ or deuterated sodium hydroxide (NaOD) using the relationship pD = pH* + 0.4 (where pH* is a direct reading in D_2O solution of the H_2O-calibrated pH meter). NMR titrations were performed by gradually adding $ZnCl_2$ dissolved in D_2O or DMSO-d_6 at 100 mM concentration to the free ligand solution directly in the NMR tube. The 1D ^1H, 1D ^{13}C, and 2D ^1H-^{13}C HSQC NMR spectra were recorded at 298.15 Kelvin on an Agilent 500/54 Premium Shielded spectrometer and on a Bruker Avance 300 Ultrashield spectrometer equipped with a double-resonance broadband probe with Z-Gradient. The 1D ^1H NMR spectra were acquired with a relaxation delay of 1.5 s, 64 scans, 32K (1K = 1024) data points, and a spectral width of 21 ppm. The 1D ^{13}C spectra were acquired with power-gated decoupling using a 20° flip angle, a waltz16 decoupling scheme, and a relaxation delay of 2.0 s. Each

spectrum consisted of 16K scans, 32K data points, and a spectral width of 300 ppm (^{13}C carrier at 130 ppm). The 2D ^1H-^{13}C HSQC experiments were acquired with an insensitive nuclei enhanced by polarization transfer (INEPT) delay 1/(4J$_{C-H}$) of 1.72 ms (J$_{C-H}$ = 145 Hz) and a recycle delay of 1.5 s. Each time-domain spectrum was the average of 64 scans consisting of 1K complex data points over a direct dimension (F2) (^1H) spectral width of 13.35 ppm; the second dimension was derived from 256 increments with an indirect dimension (F1) (^{13}C) spectral width of 250 ppm centered at 75 ppm. Decoupling during the acquisition time was achieved using a garp decoupling scheme. In addition, 2D ^1H-^1H correlated spectroscopy (COSY), total correlated spectroscopy (TOCSY), and rotating-frame nuclear Overhauser effect spectroscopy (ROESY) and 2D ^1H-^{13}C heteronuclear multiple bond correlation (HMBC) spectra were recorded for complete resonance assignment. All data were processed with Bruker software Topspin (version 3.5). Before Fourier transformation, an exponential multiplication with a line broadening of 0.30 and 2 Hz was applied for 1D ^1H and 1D ^{13}C spectra, respectively. The 2D spectral data, zero filled in F1 to 1K data points, were subjected to apodization using a squared cosine bell function in both dimensions prior to Fourier transformation and phase correction. ^1H and ^{13}C chemical shifts were referenced to trimethylsilylpropanoic acid (TSP; δ_{1H} = 0.0 ppm) for the spectra in D_2O or to residual partially deuterated DMSO (DMSO-d_5) (δ_{1H} = 2.50 ppm and δ_{13C} = 39.52 ppm) for the spectra in DMSO.

DFT Calculations. Initial structures for the Zn(II) complexes were built in Gauss-View. A first round of geometry optimizations was performed using G09 (77) to yield initial structures that would feed geometry optimizations in ORCA 4.2.1 (78). Restricted Kohn Sham calculations were performed using the empirical functional BP, the hybrid functional B3LYP, and the range separated functional ωB97X-D3 (79–81) that includes an atom pairwise dispersion correction with the zero-damping scheme (D30) (82), the orbital basis set def2-TZVP (83), and the auxiliary basis set def2/J (84, 85). Solvation was modeled using a conductor-like polarizable continuum model, with a dielectric constant of 80.4 simulating water (86). The structures obtained from ORCA were reoptimized with the Gaussian 09 program for electronic structure calculations using the same functionals and basis sets and solvation model (87) for implicit solvation modeling. With this methodology, the harmonic analysis indicates that all the optimized structures are local minima on the potential energy surface (i.e., the structures do not have imaginary frequencies) (*SI Appendix,* Table S4).

Data Availability. All study data are included in the article and/or supporting information.

1. X. Xiao, V. M. Alfaro-Magallanes, J. L. Babitt, Bone morphogenic proteins in iron homeostasis. *Bone* **138**, 115495 (2020).

2. M. U. Muckenthaler, S. Rivella, M. W. Hentze, B. Galy, A red carpet for iron metabolism. *Cell* **168**, 344–361 (2017).

3. T. Kambe, K. M. Taylor, D. Fu, Zinc transporters and their functional integration in mammalian cells. *J. Biol. Chem.* **296**, 100320 (2021).

4. J. C. Lye *et al.*, Systematic functional characterization of putative zinc transport genes and identification of zinc toxicosis phenotypes in *Drosophila melanogaster. J. Exp. Biol.* **215**, 3254–3265 (2012).

5. S. Yin, Q. Qin, B. Zhou, Functional studies of *Drosophila* zinc transporters reveal the mechanism for zinc excretion in Malpighian tubules. *BMC Biol.* **15**, 12 (2017).

6. S. Redhai *et al.*, An intestinal zinc sensor regulates food intake and developmental growth. *Nature* **580**, 263–268 (2020).

7. R. Luo *et al.*, Molecular basis and homeostatic regulation of Zinc taste. *Protein Cell*, 10.1007/s13238-021-00845-8 (2021).

8. W. Maret, Zinc in pancreatic islet biology, insulin sensitivity, and diabetes. *Prev. Nutr. Food Sci.* **22**, 1–8 (2017).

9. J. Consuegra *et al.*, *Drosophila*-associated bacteria differentially shape the nutritional requirements of their host during juvenile growth. *PLoS Biol.* **18**, e3000681 (2020).

10. K. Zierold, A. Wessing, Mass dense vacuoles in *Drosophila* Malpighian tubules contain zinc, not sodium. A reinvestigation by X-ray microanalysis of cryosections. *Eur. J. Cell Biol.* **53**, 222–226 (1990).

11. A. D. Stewart *et al.*, Distribution of metals in the termite *Tumulitermes tumuli* (Froggatt): Two types of Malpighian tubule concretion host Zn and Ca mutually exclusively. *PLoS One* **6**, e27578 (2011).

12. C. Tejeda-Guzmán *et al.*, Biogenesis of zinc storage granules in *Drosophila melanogaster. J. Exp. Biol.* **221**, jeb168419 (2018).

13. T. H. Morgan, Sex limited inheritance in *Drosophila. Science* **32**, 120–122 (1910).

14. G. W. Beadle, B. Ephrussi, The differentiation of eye pigments in *Drosophila* as studied by transplantation. *Genetics* **21**, 225–247 (1936).

15. J. R. Shoup, The development of pigment granules in the eyes of wild type and mutant *Drosophila melanogaster. J. Cell Biol.* **29**, 223–249 (1966).

16. D. T. Sullivan, M. C. Sullivan, Transport defects as the physiological basis for eye color mutants of *Drosophila melanogaster. Biochem. Genet.* **13**, 603–613 (1975).

17. J. Ferré, F. J. Silva, M. D. Real, J. L. Ménsua, Pigment patterns in mutants affecting the biosynthesis of pteridines and xanthommatin in *Drosophila melanogaster. Biochem. Genet.* **24**, 545–569 (1986).

18. V. Lloyd, M. Ramaswami, H. Krämer, Not just pretty eyes: *Drosophila* eye-colour mutations and lysosomal delivery. *Trends Cell Biol.* **8**, 257–259 (1998).

19. J. Borycz, J. A. Borycz, A. Kubów, V. Lloyd, I. A. Meinertzhagen, *Drosophila* ABC transporter mutants white, brown and scarlet have altered contents and distribution of biogenic amines in the brain. *J. Exp. Biol.* **211**, 3454–3466 (2008).

20. S. Yagi, H. Ogawa, Effect of tryptophan metabolites on fluorescent granules in the Malpighian tubules of eye color mutants of *Drosophila melanogaster. Zool. Sci.* **13**, 97–104 (1996).

21. J. Vásquez-Procopio *et al.*, Intestinal response to dietary manganese depletion in *Drosophila. Metallomics* **12**, 218–240 (2020).

22. M. D. W. Piper, Using artificial diets to understand the nutritional physiology of *Drosophila melanogaster. Curr. Opin. Insect Sci.* **23**, 104–111 (2017).

23. G. W. Evans, Normal and abnormal zinc absorption in man and animals: The tryptophan connection. *Nutr. Rev.* **38**, 137–141 (1980).

24. A. S. Prasad, Impact of the discovery of human zinc deficiency on health. *J. Trace Elem. Med. Biol.* **28**, 357–363 (2014).

25. J. C. King *et al.*, Biomarkers of Nutrition for Development (BOND)-zinc review. *J. Nutr.* **146**, 858S–885S (2015).

26. M. W. Jones, M. D. de Jonge, S. A. James, R. Burke, Elemental mapping of the entire intact *Drosophila* gastrointestinal tract. *J. Biol. Inorg. Chem.* **20**, 979–987 (2015).

27. C. Wang, A. C. Spradling, An abundant quiescent stem cell population in *Drosophila* Malpighian tubules protects principal cells from kidney stones. *eLife* **9**, e54094 (2020).

28. G. Wellenreuther, M. Cianci, R. Tucoulou, W. Meyer-Klaucke, H. Haase, The ligand environment of zinc stored in vesicles. *Biochem. Biophys. Res. Commun.* **380**, 198–203 (2009).

29. S. A. Thomas, B. Mishra, S. C. B. Myneni, High energy resolution-X-ray absorption near edge structure spectroscopy reveals Zn ligation in whole cell bacteria. *J. Phys. Chem. Lett.* **10**, 2585–2592 (2019).

30. V. V. Yanshole *et al.*, Photoinduced tautomeric transformations of xanthurenic acid. *Phys. Chem. Chem. Phys.* **12**, 9502–9515 (2010).

31. C. Talmard, A. Bouzan, P. Faller, Zinc binding to amyloid-beta: Isothermal titration calorimetry and Zn competition experiments with Zn sensors. *Biochemistry* **46**, 13658–13666 (2007).

32. Z. Xiao, A. G. Wedd, The challenges of determining metal-protein affinities. *Nat. Prod. Rep.* **27**, 768–789 (2010).

33. H. Yepiskoposyan *et al.*, Transcriptome response to heavy metal stress in *Drosophila* reveals a new zinc transporter that confers resistance to zinc. *Nucleic Acids Res.* **34**, 4866–4877 (2006).

34. T. M. Rizki, R. M. Rizki, An inducible enzyme system in the larval cells of *Drosophila melanogaster. J. Cell Biol.* **17**, 87–92 (1963).

35. S. Kashio, M. Miura, Kynurenine metabolism in the fat body non-autonomously regulates imaginal disc repair in *Drosophila. iScience* **23**, 101738 (2020).

36. Y. Naya, M. Ohnishi, M. Ikeda, W. Miki, K. Nakanishi, What is molt-inhibiting hormone? The role of an ecdysteroidogenesis inhibitor in the crustacean molting cycle. *Proc. Natl. Acad. Sci. U.S.A.* **86**, 6826–6829 (1989).

37. S. J. F. Cronin *et al.*, The metabolite BH4 controls T cell proliferation in autoimmunity and cancer. *Nature* **563**, 564–568 (2018).

38. L. F. Campesato *et al.*, Blockade of the AHR restricts a Treg-macrophage suppressive axis induced by L-Kynurenine. *Nat. Commun.* **11**, 4011 (2020).

39. C. C. Clement *et al.*, 3-Hydroxy-L-kynurenamine is an immunomodulatory biogenic amine. *Nat. Commun.* **12**, 4447 (2021).

40. I. Wessels, H. J. Fischer, L. Rink, Dietary and physiological effects of zinc on the immune system. *Annu. Rev. Nutr.* **41**, 133–175 (2021).

41. G. W. Evans, E. C. Johnson, Zinc absorption in rats fed a low-protein diet and a low-protein diet supplemented with tryptophan or picolinic acid. *J. Nutr.* **110**, 1076–1080 (1980).

42. L. S. Hurley, B. Lönnerdal, Tryptophan, picolinic acid and zinc absorption: An unconvincing case. *J. Nutr.* **110**, 2536–2538 (1980).

43. A. Wadano, Y. Takenaka, M. Matumoto, 3-Hydroxykynurenine as a radical scavenger in the blowfly, *Aldrichina grahami. Insect Biochem. Mol. Biol.* **23**, 919–925 (1993).

44. F. Figon *et al.*, Catabolism of lysosome-related organelles in color-changing spiders supports intracellular turnover of pigments. *Proc. Natl. Acad. Sci. U.S.A.* **118**, e2103020118 (2021).

45. B. J. Earley, A. D. Mendoza, C.-H. Tan, K. Kornfeld, Zinc homeostasis and signaling in the roundworm C. elegans. *Biochim. Biophys. Acta Mol. Cell Res.*1868,118882 (2021).

46. F. Husnik, V. Hypsa, A. Darby, Insect-symbiont gene expression in the midgut bacteriocytes of a blood-sucking parasite. *Genome Biol. Evol.* **12**, 429–442 (2020).

47. S. Haq, J. A. Grondin, W. I. Khan, Tryptophan-derived serotonin-kynurenine balance in immune activation and intestinal inflammation. *FASEB J.* **35**, e21888 (2021).

48. L. Laurans *et al.*, Genetic deficiency of indoleamine 2,3-dioxygenase promotes gut microbiota-mediated metabolic health. *Nat. Med.* **24**, 1113–1120 (2018).

49. S. A. Worton *et al.*, Kynurenine relaxes arteries of normothensive women and those with preeclampsia. *Circ. Res.* **128**, 1679–1693 (2021).

50. F. Fazio *et al.*, Vasorelaxing action of the kynurenine metabolite, xanthurenic acid: The missing link in endotoxin-induced hypotenstion? *Front. Pharmacol.* **8**, 214 (2017).

51. A. H. Betrie *et al.*, Zinc drives vasorelaxation by acting in sensory nerves, endothelium and smooth muscle. *Nat. Commun.* **12**, 3296 (2021).

52. S. Campesan *et al.*, The kynurenine pathway modulates neurodegeneration in a *Drosophila* model of Huntington's disease. *Curr. Biol.* **21**, 961–966 (2011).

53. A. V. Zhuravlev, O. V. Vetrovoy, P. N. Ivanova, E. V. Savvateeva-Popova, 3-Hydroxykynurenine in regulation of *Drosophila* behavior: The novel mechanisms for *cardinal* phenotype manifestations. *Front. Physiol.* **11**, 971 (2020).

54. D. Wilinski *et al.*, Rapid metabolic shifts occur during the transition between hunger and satiety in *Drosophila melanogaster. Nat. Commun.* **10**, 4052 (2019).

55. G. F. Oxenkrug, V. Navrotskaya, L. Voroboyva, P. Summergrad, Extension of life span of *Drosophila melanogaster* by the inhibitors of tryptophan-kynurenine metabolism. *Fly (Austin)* **5**, 307–309 (2011).

56. C. Coburn, D. Gems, The mysterious case of the C. elegans gut granule: Death fluorescence, anthranilic acid and the kynurenine pathway. *Front. Genet.* **4**, 151 (2013).

57. A. Sasaki, T. Nishimura, T. Takano, S. Naito, S. K. Yoo, white regulates proliferative homeostasis of intestinal stem cells during ageing in *Drosophila. Nat. Metab.* **3**, 546–557 (2021).

58. M. Granold, P. Hajieva, M. I. Toşa, F. D. Irimie, B. Moosmann, Modern diversification of the amino acid repertoire driven by oxygen. *Proc. Natl. Acad. Sci. U.S.A.* **115**, 41–46 (2018).

59. R. J. P. Williams, Zinc in evolution. *J. Inorg. Biochem.* **111**, 104–109 (2012).

60. C. L. Dupont, A. Butcher, R. E. Valas, P. E. Bourne, G. Caetano-Anollés, History of biological metal utilization inferred through phylogenomic analysis of protein structures. *Proc. Natl. Acad. Sci. U.S.A.* **107**, 10567–10572 (2010).

61. Y. Yasui *et al.*, Analysis of the predictive factors for a critical illness of COVID-19 during treatment - relationship between serum zinc level and critical illness of COVID-19. *Int. J. Infect. Dis.* **100**, 230–236 (2020).

62. D. Jothimani *et al.*, COVID-19: Poor outcomes in patients with zinc deficiency. *Int. J. Infect. Dis.* **100**, 343–349 (2020).

63. W. Xu *et al.*, Hypozincemia in COVID-19 patients correlates with stronger antibody response. *Front. Immunol.* **12**, 785599 (2022).

64. B. Shen *et al.*, Proteomic and metabolomic characterization of COVID-19 patient sera. *Cell* **182**, 59–72.e15 (2020).

65. T. Thomas *et al.*, COVID-19 infection alters kynurenine and fatty acid metabolism, correlating with IL-6 levels and renal status. *JCI Insight* **5**, e140327 (2020).

66. J. Guo *et al.*; Amsterdam UMC COVID-19 Biobank Study Group, Indoleamine 2,3-dioxygenase (IDO)-1 and IDO-2 activity and severe course of COVID-19. *J. Pathol.* **256**, 256–261 (2022).

67. H. Mangge *et al.*, Increased kynurenine indicates a fatal course of COVID-19. *Antioxidants* **10**, 1960 (2021).

68. E. Cohen, J. K. Sawyer, N. G. Peterson, J. A. T. Dow, D. T. Fox, Physiology, development, and disease modeling in the *Drosophila* excretory system. *Genetics* **214**, 235–264 (2020).

69. L. A. Perkins *et al.*, The Transgenic RNAi Project at Harvard Medical School: Resources and Validation. *Genetics* **201**, 843–852 (2015).

70. G. Weitzel, E. Buddecke, F. J. Strecker, U. Roester, [Zinc binding capacity and glycemic effect of xanthurenic acid kynurenine and tryptophan]. *Hoppe Seylers Z. Physiol. Chem.* **298**, 169–184 (1954).

71. N. Schuth *et al.*, Effective intermediate-spin iron in O₂-transporting heme proteins. *Proc. Natl. Acad. Sci. U.S.A.* **114**, 8556–8561 (2017).

72. A. Petuker *et al.*, Spontaneous Si-C bond cleavage in (TriphosSi)-nickel complexes. *Dalton Trans.* **46**, 907–917 (2017).

73. O. Müller, M. Nachtegaal, J. Just, D. Lützenkirchen-Hecht, R. Frahm, Quick-EXAFS setup at the SuperXAS beamline for in situ X-ray absorption spectroscopy with 10 ms time resolution. *J. Synchrotron Radiat.* **23**, 260–266 (2016).

74. A. L. Ankudinov, B. Ravel, J. J. Rehr, S. D. Conradson, Real space multiple scattering calculation of XANES. *Phys. Rev.* **58**, 7565 (1998).

75. J. Dittmer, H. Dau, Theory of the linear dichroism in the extended X-ray absorption fine structure (EXAFS) of partially vectorially ordered systems. *J. Phys. Chem. B* **102**, 8196–8200 (1998).

76. H. Dau, P. Liebisch, M. Haumann, X-ray absorption spectroscopy to analyze nuclear geometry and electronic structure of biological metal centers–Potential and questions examined with special focus on the tetra-nuclear manganese complex of oxygenic photosynthesis. *Anal. Bioanal. Chem.* **376**, 562–583 (2003).

77. M. J. Frisch *et al.*, Gaussian 16 (Revision C.01, Gaussian, Inc., Wallingford, CT, 2016).

78. F. Neese, Software update: The ORCA program system, version 4.0. *Wiley Interdiscip. Rev. Comput. Mol. Sci.* **8**, e1327 (2017).

79. A. D. Becke, Density-functional exchange-energy approximation with correct asymptotic behavior. *Phys. Rev. A Gen. Phys.* **38**, 3098–3100 (1988).

80. J. P. Perdew, Density-functional approximation for the correlation energy of the inhomogeneous electron gas. *Phys. Rev. B Condens. Matter* **33**, 8822–8824 (1986).

81. J. D. Chai, M. Head-Gordon, Long-range corrected hybrid density functionals with damped atom-atom dispersion corrections. *Phys. Chem. Chem. Phys.* **10**, 6615–6620 (2008).

82. S. Grimme, J. Antony, S. Ehrlich, H. Krieg, A consistent and accurate ab initio parametrization of density functional dispersion correction (DFT-D) for the 94 elements H-Pu. *J. Chem. Phys.* **132**, 154104 (2010).

83. F. Weigend, R. Ahlrichs, Balanced basis sets of split valence, triple zeta valence and quadruple zeta valence quality for H to Rn: Design and assessment of accuracy. *Phys. Chem. Chem. Phys.* **7**, 3297–3305 (2005).

84. F. Weigend, Accurate Coulomb-fitting basis sets for H to Rn. *Phys. Chem. Chem. Phys.* **8**, 1057–1065 (2006).

85. F. Neese, F. Wennmohs, A. Hansen, U. Becker, Efficient, approximate and parallel Hartree-Fock and hybrid DFT calculations. A 'chain-of-spheres' algorithm for the Hartree-Fock exchange. *Chem. Phys.* **365**, 98–109 (2009).

86. V. Barone, M. Cossi, Quantum calculation of molecular energies and energy gradients in solution by a conductor solvent model. *J. Phys. Chem. A* **102**, 1995–2001 (1998).

87. A. V. Marenich, C. J. Cramer, D. G. Truhlar, Universal solvation model based on solute electron density and on a continuum model of the solvent defined by the bulk dielectric constant and atomic surface tensions. *J. Phys. Chem. B* **113**, 6378–6396 (2009).